

RESEARCH ARTICLE

10.1002/2017WR021015

Key Points:

- Generated precipitation fields are consistent with observed Microwave Link rain rates and rain gauge measurements
- Fields additionally reflect the observed rainfall variability along the Microwave Link paths
- Ensemble spread of reconstructed precipitation fields enables uncertainty estimation

Correspondence to:

B. Haese,
barbara.haese@geo.uni-augsburg.de

Citation:

Haese, B., Hörning, S., Chwala, C., Bárdossy, A., Schälge, B., & Kunstmann, H. (2017). Stochastic reconstruction and interpolation of precipitation fields using combined information of commercial microwave links and rain gauges. *Water Resources Research*, 53, 10,740–10,756. <https://doi.org/10.1002/2017WR021015>

Received 27 APR 2017

Accepted 23 NOV 2017

Accepted article online 29 NOV 2017

Published online 22 DEC 2017

Stochastic Reconstruction and Interpolation of Precipitation Fields Using Combined Information of Commercial Microwave Links and Rain Gauges

B. Haese¹ , S. Hörning² , C. Chwala³ , A. Bárdossy⁴ , B. Schälge⁵ , and H. Kunstmann^{1,3} 
¹Institute of Geography, University of Augsburg, Augsburg, Germany, ²School of Earth and Environmental Sciences, University of Queensland, Brisbane, Australia, ³Institute of Meteorology and Climate Research (IMK-IFU), Karlsruhe Institute of Technology (KIT), Garmisch-Partenkirchen, Germany, ⁴Institute for Modelling Hydraulic and Environmental Systems, University of Stuttgart, Stuttgart, Germany, ⁵Meteorological Institute, University of Bonn, Bonn, Germany

Abstract For the reconstruction and interpolation of precipitation fields, we present the application of a stochastic approach called Random Mixing. Generated fields are based on a data set consisting of rain gauge observations and path-averaged rain rates estimated using Commercial Microwave Link (CML) derived information. Precipitation fields are received as linear combination of unconditional spatial random fields, where the spatial dependence structure is described by copulas. The weights of the linear combination are optimized such that the observations and the spatial structure of the precipitation observations are reproduced. The innovation of the approach is that this strategy enables the simulation of ensembles of precipitation fields of any size. Each ensemble member is in concordance with the observed path-averaged CML derived rain rates and additionally reflects the observed rainfall variability along the CML paths. The ensemble spread allows additionally an estimation of the uncertainty of the reconstructed precipitation fields. The method is demonstrated both for a synthetic data set and a real-world data set in South Germany. While the synthetic example allows an evaluation against a known reference, the second example demonstrates the applicability for real-world observations. Generated precipitation fields of both examples reproduce the spatial precipitation pattern in good quality. A performance evaluation of Random Mixing compared to Ordinary Kriging demonstrates an improvement of the reconstruction of the observed spatial variability. Random Mixing is concluded to be a beneficial new approach for the provision of precipitation fields and ensembles of them, in particular when different measurement types are combined.

1. Introduction

Knowledge of the spatiotemporal distribution of rainfall is crucial for the understanding of the regional water cycle. Since precipitation has a high variability both in space and time, the available spatiotemporal products often still suffer from limited quality. Precipitation fields derived from atmospheric models can suffer from significant limitations concerning the reproduction of the spatiotemporal distribution of rainfall fields (e. g., Frei et al., 2003; Randall et al., 2007; Smiatek et al., 2016). Stochastic precipitation fields conditioned on observations are assumed to be more reliable, even when considering measurement uncertainties.

Most common are observations from rain gauge stations, which provide high-quality information for a specific measurement point. Their main disadvantage is the limited spatial representativeness, which can lead to significant biases in interpolated rainfall fields in particular in complex terrain. Additional uncertainties can be caused by wind or exposure-induced errors (e. g., Nešpor & Sevruk, 1999; Sevruk & Zahlavova, 1994).

A further prevalent source of precipitation information is weather radars. They provide measurements with a fairly high spatial resolution, depending on the radar system and the distance from the radar, but typically in the range of 1 km. The accuracy of weather radar measurements, however, suffers from the uncertainty of the relation between the measured reflectivity Z and the desired quantity, the rain rate R (Ulbrich & Lee, 1999). Additional errors are induced by the effect of the vertical profile of reflectivity (e. g., Hazenberg et al., 2011; Joss & Pittini, 1991), beam blockage, and bright band interception (e. g., Andrieu et al., 1997; Germann et al., 2006; Wagner et al., 2012). The latter two are particularly present in mountain areas. In order to reduce the uncertainties induced by the complex relation between reflectivity and precipitation, radar observations

are combined with rain gauge measurements. Combining methods range from Mean Field Bias correction (e. g., Seo & Breidenbach, 2002; Thorndahl et al., 2014), over various geostatistical approaches (e. g., Goudenhoofd & Delobbe, 2009), to nonparametric approaches (e. g., Hasan et al., 2016a, 2016b). Hasan et al. (2016a) showed recently that in case of a large available amount of data such nonparametric merging approaches are less sensitive to the effects of the vertical reflectivity profile.

The technique of exploiting data from existing CML networks was introduced as an alternative method for rainfall estimations by Messer et al. (2006). This technique relies on the fact that precipitation attenuates the microwave radiation along the path between a transmitting to a receiving antenna. The observed attenuation A in dB can be related to a path-averaged rain rate (\bar{R}) via the relation $A = a(\bar{R})^b L = a \int_L r(x)^b dx$ (Olsen et al., 1978), where L is the length of the CML and a , b are constants depending on the radiation frequency and on the rain drop-size distribution (DSD) (Jameson, 1991). Compared to the Z-R relation of the weather radar, this A-R relation is relatively robust to changes in the DSD, in particular in the frequency band between 20 and 40 GHz, which is typical for CMLs. One further advantage of CMLs is that there already exist large networks of them in almost all inhabited areas around the globe (Global System for Mobile Communications, 2017, available at <http://www.gsma.com/aboutus/gsm-technology/gsm>). Uncertainties are induced for example by wet antennas or the spatial variability of the assumed DSD along the link path (e. g., Berne & Uijlenhoet, 2007; Leijnse et al., 2008; Overeem et al., 2011).

Several studies have shown the successful usage of CMLs for rainfall estimations (e. g., Chwala et al., 2012; Doumounia et al., 2014; Overeem et al., 2011; Zinevich et al., 2010). The potential of such rainfall estimations for hydrological model simulations has recently been shown by Smiatek et al. (2017). Bianchi et al. (2013) have introduced an assimilation based method to obtain rain rate information by combining rain gauge, radar, and microwave link observations. The reconstruction of spatiotemporal precipitation dynamics by assimilating a rainfall advection model and CML observations is shown by Zinevich et al. (2008b). Liberman et al. (2014b) have improved radar-based rainfall mapping by integrating CML information. In addition, various approaches exist which aim at 2-D precipitation field reconstructions based on CMLs, e. g., (Overeem et al., 2013, 2016) have assigned the CML measurement as point information on the center of the links and have interpolated this data using Ordinary Kriging or Inverse Distance Weighting. Based on the work of (Giuli et al., 1991, 1999), e. g., Zinevich et al. (2008a) and D'Amico et al. (2016) have reconstructed precipitation fields utilizing CMLs using a tomographic model. Further approaches divide each link into subsegments and achieve the rain rates of the subsegments by e. g., a sampling algorithm (Goldshtein et al., 2009), an iterative Newton-Raphson algorithm (Liberman & Messer, 2014a), or a measurement model (Roy et al., 2014). Subsequently the authors use these estimates for the reconstruction of the rainfall pattern.

In this study, we apply the stochastic Random Mixing method (Bárdossy & Hörning, 2015) on a combined data set of rain gauge and CML precipitation measurements to reconstruct precipitation fields. Following this method, a precipitation field is received as a linear combination of unconditional spatial random fields in which the spatial dependence structure is described by copulas. By varying the weights of the linear combination such fields are generated which reproduce the observations and the observed spatial structure. One advantage of Random Mixing is that this linear combination is directly constrained by the observations, thereby the rain gauge observations are linear constraints and the CML observations are nonlinear ones. This implies that the CML measurements have not to be transformed into point or pixel information. Since the equation system given by the linear combination and its constraints has not a unique solution, Random Mixing has the benefit of generating ensembles of possible reconstructions. Each ensemble member is in concordance with the combined observational data and reflect the observed rainfall variability. Especially, each field reflects the observed rain rates but the precipitation values along the CML paths vary within the ensemble. Moreover, such ensembles of reconstructed rainfall fields allow additionally an uncertainty estimation.

For the evaluation of precipitation fields generated by Random Mixing, we utilize as a first example a synthetic data set based on a virtual reality (VR): Rain gauge observations and CML measurements are generated from an atmospheric model simulation of the Neckar catchment. In this case, the model simulation represents the VR in which synthetic observations allow to mimic advantages and disadvantages of real observations. This VR setup enables a detailed evaluation of the reconstructed or interpolated precipitation fields, including a comparison to the existing algorithm of Overeem et al. (2013), against the known reference. A second example demonstrates the applicability of Random Mixing to real observations. Here, the

interpolation is based on rain gauge observations provided by DWD Climate Data Center (CDC) and real-time data of CML networks acquired with the system introduced by Chwala et al. (2016). Due to the current availability of CML measurements, the applicability to real observations for the Neckar catchment was not yet feasible. Instead we have chosen a neighboring area for the second example. As reference for the evaluation of the real-world example, we use the so-called RADOLAN RW data set (Radar Online Calibration), a radar product generated by the CDC (Bartels et al., 2004).

2. Method

The idea of Random Mixing is an extension of the Gradual Deformation approach first presented by Hu (2000). It has been shown that any spatially normally distributed random field $Z(x)$ can be expressed as a linear combination of n independent random fields $Y_i(x)$ with the corresponding weights α_i :

$$Z(x) = \sum_{i=1}^n \alpha_i Y_i(x) \quad (1)$$

The expected value (E) of this field $Z(x)$ has to be 0 with $E[Z(x)] = E[Y_i(x)] = 0$, and the variance (Var) is $Var[Z(x)] = Var[Y_i(x)] = 1$. Thereby the spatial distribution of these random fields is described by the covariance matrix Γ . For the construction of the covariance of the linear combination, it is assumed that all $Y_i(x)$ share the same covariance $\Gamma_{Y_i(x)}$ and that:

$$\sum_{i=1}^n \alpha_i^2 = 1 \quad (2)$$

If equation (2) is satisfied, it follows $\Gamma_{Z(x)} = \Gamma_{Y_i(x)}$.

While Hu (2000) requires a normally distributed random field $Z(x)$, Bárdossy and Hörning (2015) showed that this requirement can be weakened by the assumption that the spatial dependence of $Z(x)$ can be represented by Gaussian copulas. The advantage of copulas is the ability to describe the dependence structure independent of the marginal distribution. A detailed introduction can be found in Nelsen (1999). The application of copulas for hydrometeorological problems was successfully shown in e.g., Bárdossy and Pegram (2013), Laux et al. (2011), Mao et al. (2015), Serinaldi (2009), and Vogl et al. (2012).

This study aims at the reconstruction of spatial precipitation fields $R(x)$ based on rain gauge and path averaged CML observations. Precipitation is usually not spatially normally distributed hence the field $R(x)$ does not fulfill the requirement of Hu (2000). Using the advantage of the copula approach, the precipitation field $R(x)$ can be transformed into a normally distributed field $Z(x)$. The resulting field $Z(x)$ fulfills the weakened requirement for the use of Random Mixing. When $F(r)$ denotes the marginal distribution of the precipitation field $R(x)$ and Φ^{-1} is the inverse standard normal distribution, then this transformation into a normally distributed field can be described by $Z(x) = \Phi^{-1}(F(r))$.

Following the methodology proposed in Bárdossy and Hörning (2015), the construction of such a field $Z(x)$ can be realized by a stepwise procedure. Assuming that the rain gauge observations represent the frequencies of precipitation amounts of the field $R(x)$, as a first step the marginal distribution $F(r)$ is estimated based on the rain gauge observations $R(x_k)$ at locations x_k with $k \in [1 \dots K]$. K denotes the amount of rain gauge stations. Afterward the transformation of the rain gauge observations $R(x_k)$ into a normally distributed variable is performed using $z_k = \Phi^{-1}(F(R(x_k)))$. Based on the transformed observations z_k , a Gaussian copula model, reflecting the spatial dependence structure of the rain gauge observations, is constructed. The construction of such a copula model has been described in Bárdossy and Li (2008). This copula model is used to simulate n unconditional random fields $Y_i(x)$ with $i \in [1 \dots n]$.

Subsequently, one has to find such α_i that $Z(x)$ satisfies the rain gauge observations. This can be expressed by the linear system:

$$Z(x_k) = \sum_{i=1}^n \alpha_i Y_i(x_k) = z_k, \quad (3)$$

for all $k \in [1, \dots, K]$. If n , with $n > K$, is large enough, equation (3) has infinite solutions. However, not all solutions necessarily satisfy equation (2). Therefore Bárdossy and Hörning (2015) suggested to find a solution of

equation (3) in which the sum of the squared weights α_i is minimized with a minimum much smaller than one:

$$\sum_{i=1}^n (\alpha'_i)^2 \ll 1. \quad (4)$$

Equations (3) and (4) describe the quadratic optimization problem $\arg \min_{[\alpha'_1, \dots, \alpha'_n]} \sum_{i=1}^n (\alpha'_i)^2$, which can be easily solved. If this minimum is larger than 1, n , the number of unconditional fields $Y_i(x)$, will be increased until a minimum much smaller than 1 is found. The resulting field

$$Z'(x) = \sum_{i=1}^n \alpha'_i Y_i(x) \quad (5)$$

solves equation (3) and consequently reproduces the rain gauge observations, but has a much lower variance as the target field $Z(x)$. Therefore $Z'(x)$ is called a quasi-interpolation.

To preserve the variance of $Z(x)$ a second component $Z''(x)$, which is also expressed by a linear combination, has to be added. Each addend $U_m(x)$ with $m \in [1, \dots, J-K]$ of $Z''(x)$ has to fulfill

$$U_m(x_k) = 0 \quad (6)$$

for each rain gauge observation $k \in [1, \dots, K]$. Consequently, any linear combination of $U_m(x)$ added to $Z'(x)$ will fulfill equation (3).

Each field $U_m(x)$ will also be constructed as a linear combination of $J(J > K)$ unconditional fields. These fields have the same spatial properties as $Y_i(x)$. The construction of the U_m is explained in more detail by Bárdossy and Hörning (2015). Consequently, $Z''(x)$ can be specified as the following homogeneous system:

$$Z''(x) = p(\alpha', \lambda) \sum_{m=1}^{J-K} \lambda_m U_m(x) \quad (7)$$

with the corresponding weights λ_m for the U_m . The function $p(\alpha', \lambda)$ is a function of the weight vectors $\alpha' = (\alpha'_i)_{i \in \{1, \dots, n\}}$ and $\lambda = (\lambda_m)_{m \in \{1, \dots, J-K\}}$ which map into \mathbb{R} . Function p is designed in such way that the combined weights of the sum $Z(x) = Z'(x) + Z''(x)$ solve equation (2) (Bárdossy & Hörning, 2015). The main advantage of this construction is that one can generate an infinite number of conditional fields by modifying the weights λ_m . Particularly by varying λ_m fields $Z(x)$ can be constructed which are in concordance with the observed path averaged CML rain rates \bar{R} .

In order to find such λ_m the observed rain rates, \bar{R} have to be compared with the corresponding values of the field $Z(x)$. Therefore, for each CML path L_ξ , with $\xi \in [1, \dots, \Xi]$ and Ξ denoting the amount of CMLs, the path-averaged rain rate of the field $Z(x)$ is calculated as:

$$\int_{L_\xi} F^{-1}(\Phi(Z(x))) dx. \quad (8)$$

Here, Φ is the standard normal distribution and F^{-1} the inverse marginal distribution. The comparison between the observed CML values \bar{R}_ξ and the corresponding path-averaged rain rates of $Z(x)$ (equation (8)) formulate nonlinear conditions. These nonlinear conditions can be achieved by minimizing the distance between the observed path averaged CML rain rates and the corresponding path integrated rain rates of the field $Z(x)$:

$$f_{obj} := \sum_{\xi=1}^{\Xi} \left(\int_{L_\xi} F^{-1}(\Phi(Z(x))) dx - \bar{R}_\xi \right)^2 < \varepsilon. \quad (9)$$

Here, f_{obj} denotes the objective function and ε a defined threshold. Until a set of weights $(\lambda_1, \dots, \lambda_{J-K})$ which minimizes the objective function with $f_{obj} < \varepsilon$ has been found, J has to be increased. The resulting field

$$Z(x) = \sum_{i=1}^n \alpha'_i Y_i(x_k) + p(\alpha', \lambda) \sum_{m=1}^{J-K} \lambda_m U_m(x) \quad (10)$$

solves equations (2) and (3) and is in concordance with the CML observations.

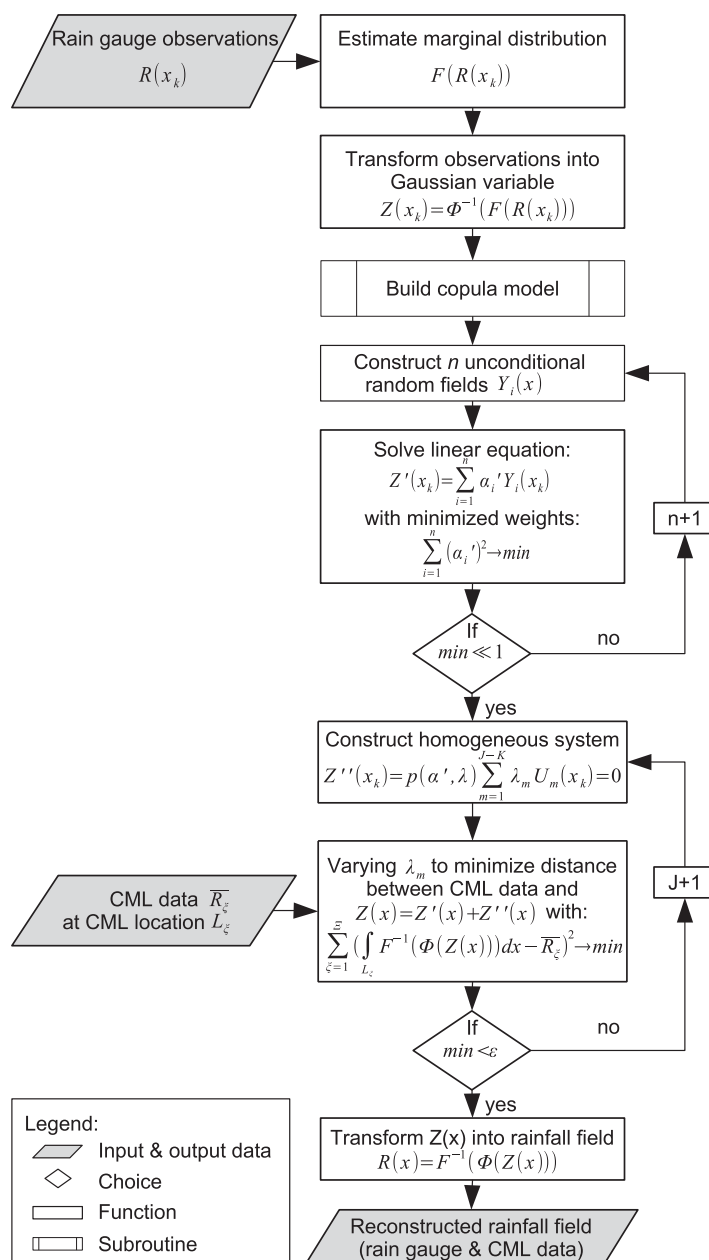


Figure 1. Flowchart of the Random Mixing algorithm.

The back transformed field $R(x) = F^{-1}(\Phi(Z(x)))$ is one possible reconstruction of the spatial precipitation field based on the given rain gauge and CML observations. One has to be aware that for each choice of the random fields $Y_i(x)$ and terms of the sum of the U_m the resulting field $Z(x)$ and thus $R(x)$ could be different. Hence, by using Random Mixing one can generate ensembles of random fields which agree with the observations with any count of ensemble members. Figure 1 shows the flowchart of the method.

3. Data

3.1. Synthetic Data Set

The synthetic data set is generated from the Consortium for Small-Scale Modeling (COSMO v4.21) model (Baldauf et al., 2011) coupled to the Community Land Model (CLM), a land-surface model (Lawrence & Chase, 2007). The COSMO model is a nonhydrostatic numerical weather prediction model, which is based on thermo-hydrodynamical equations. Since COSMO is a limited-area model, it needs lateral boundary conditions. These are provided by the COSMO-DE model which is run with a horizontal resolution of 2.8 km spanning the whole of Germany. The lateral boundary forcing as well as the constant fields (topography, land-mask etc.) are downscaled to a 1.1 km grid by linear interpolation. For the atmosphere forcing, the lateral boundary conditions are nudged against the internal model solution. This is done over a transition of a 12 km zone between the two domains. The resulting domain for our precipitation fields cover a rectangular area of approx. 57,850 km², with a horizontal resolution of approx. 1.1 km (0.01° in rotated COSMO latitude-longitude coordinates), which includes the whole Neckar catchment of approx. 14,000 km², located in South Germany. After a spin up of 100 model days (each day is forced with the atmospheric data from 1 January 2007), the simulation period is run from 2007 to 2013. To avoid boundary issues, we restrict our interpolation area of the catchment from 47.8°N to 49.63°N and 7.95°W to 10.37°W (Figure 2, grey box). In the following, we call the synthetic data set the VR. From this VR, we extract virtual hourly observations which mimic rain gauge observations ($K = 71$, yellow dots in Figure 2) and CML precipitation estimations ($\Xi = 53$, yellow lines in Figure 2).

3.2. Real-World Observations

The real-world CML observations are located in the area from 47.95°N to 48.60°N and 10.32°W to 11.5°W (Figure 2, dashed box). In this region, data for 67 CMLs ($\Xi = 67$) are available with 1 min temporal resolution via the data acquisition system developed and continuously operated

by Chwala et al. (2016). To derive rainfall information from the raw CML data, i.e., the transmitted (TX) and received signal (RX) levels, the acquired time series are processed using the method introduced by Schleiss and Berne (2010) to identify rainy periods. The required parameters (a window length and a threshold) have been set based on findings from a comparison between CML data and radar data, performed for a different period. Hence, the parameters are not optimized for the individual CMLs and individual rain events. This may introduce false-positive or false-negative errors in the detection of the rainy periods, but guarantees that the CML data processing is independent from the rain gauge and radar measurements also used in this study. A window length value of 50 min was used for all CMLs and the threshold value was set to 0.5 dB for CMLs with constant TX level and to 0.8 dB for CMLs with variable TX level. This distinction is necessary, since the variable TX level is noisier than the received signal level, due to coarser quantization of the recorded values, 1 dB for TX, 0.3 dB for RX records. In a subsequent step, the rain rate is calculated from attenuation using the standard relation provided by the International Telecommunication Union.

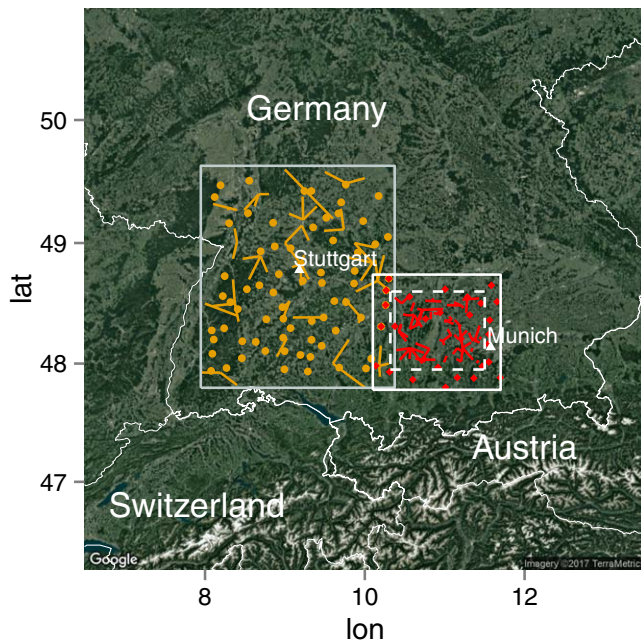


Figure 2. Description of the observational data sets: The grey box marks the area which is used for the synthetic example, the virtual observations consists of 71 synthetic rain gauges (yellow dots) and 53 synthetic CMLs (yellow lines). The solid white box marks the interpolation area of the real-world example; the observations consist of 29 rain gauges operated by the CDC (red diamonds), and 67 CMLs operated from Ericsson (red lines). The dashed box marks the area of the CML locations.

The rain gauge measurements, which are combined with the CLM data, are provided by the CDC (DWD Climate Data Center (CDC), 2016). For the specific time interval in this study, data of 11 observational stations are available within the area of the CML locations. In order to base the spatial distribution on more points, we extend our catchment area to 47.78°N to 48.74°N and 10.1°W to 11.7°W (Figure 2, solid white lined box), in which data of 29 observational stations are available ($K = 29$, red diamonds in Figure 2). Since the CDC provides hourly data sets for the rain gauges, we integrate the CLM data to a hourly data set.

3.3. RADOLAN RW Precipitation

As reference for evaluation of the real-world example, we use the so-called RADOLAN RW data set (Radar Online Calibration), which is also a CDC product (DWD CDC, 2016). The RADOLAN RW data set provides precipitation information with an 1 km spatial and an hourly (h) temporal resolution. The RADOLAN RW precipitation product is based on a quality-controlled radar composite from 17 German weather radars and adapted to hourly rain gauge observations. This routine procedure has been developed within the RADOLAN project (Bartels et al., 2004) by the German Weather Service (DWD) in cooperation with the water management administrations of the federal states (LAWA) and operates since June 2005. We are aware that the RADOLAN RW data set has its own uncertainties due to the measurements itself as well as to the composing process. However, since the RADOLAN RW data set is a widely used reference for precipitation pattern estimations (e. g., Kühnlein et al., 2014; Philipp et al., 2016; Weijenborg et al., 2015), we use this data set for the evaluation of advantages and disadvantages of the Random Mixing method.

4. Examples and Evaluations

Both examples, based on synthetic and on real observations, are utilizing a chosen precipitation event. Within these examples, for each time step we are generated 75 single realizations of possible solutions of the reconstructed precipitation field. An overview of the setup can be found in the Appendix A.

For evaluation the reconstructed precipitation fields using Random Mixing are compared to the corresponding reference fields as well as to interpolated rainfall fields using the method proposed by Overeem et al. (2013). They are assigned the observed path-averaged rain rates R_{Ξ} as point observations of the center of each link. Subsequently all observation points are interpolated using Ordinary Kriging. In the following, fields generated using Random Mixing are denoted with RM and fields are interpolated using the Ordinary Kriging based method proposed by Overeem et al. (2013) are denoted with OK.

The performance of both methods is evaluated using the Root-Mean-Square Error (RMSE), the correlation coefficient (ρ), and the coefficient of determination (r^2):

$$RMSE = \sqrt{\frac{1}{n} \sum_{i=1}^n (R_{sim}^i - R_{ref}^i)^2} \quad (11)$$

$$\rho = \frac{cov(R_{sim}, R_{ref})}{\sigma_{sim} \sigma_{ref}} \quad (12)$$

$$r^2 = \frac{\sum_{i=1}^n (R_{sim}^i - \text{mean}(R_{ref}^i))^2}{\sum_{i=1}^n (R_{ref}^i - \text{mean}(R_{ref}^i))^2} \quad (13)$$

Here R_{sim} denotes the precipitation fields generated using RM or OK and R_{ref} is the corresponding reference precipitation fields, σ is the standard deviation, and cov is the covariance.

The quality measures stated above present a pixel-wise comparison between two fields which result in case of slightly displaced patterns in a double penalty error. Therefore we choose as an additional quality measure the Fraction Skill Score (FSS) (Roberts & Humphrey, 2008). The FSS is a fuzzy verification measure which compares the fractional precipitation coverage of a certain precipitation amount (threshold) for two patterns. For a chosen threshold, which defines the rainy grid cells, the FSS is calculated by:

$$FSS = 1 - \frac{\sum_{i,j=1}^N \left((P_{ref})_{ij} - (P_{sim})_{ij} \right)^2}{\sum_{i,j=1}^N (P_{ref})_{ij}^2 + \sum_{i,j=1}^N (P_{sim})_{ij}^2} \quad (14)$$

Here P_{ref} and P_{sim} are the fractional reference (ref) and reconstructed (sim) precipitation areas in each neighborhood, and N describes the neighborhood size with the indices i and j for pixels into longitude and latitude direction. The FSS values for each threshold and neighborhood size range between 0 and 1 (perfect coverage). If the FSS value passes $0.5 + \frac{f_{ref}}{2}$, a reasonable skill is achieved. Here f_{ref} is the wet-area ratio of the reference field.

4.1. Synthetic Test Case

The first example is the synthetic test case based on the VR. Utilizing the VR, we generate faultless hourly observations, 71 virtual rain gauge and 53 virtual CML observations. For demonstration we choose a precipitation event which lasted over 4 days (from 6 P.M. on 30 May 2013 until 1 A.M. on 2 June 2013). Based on

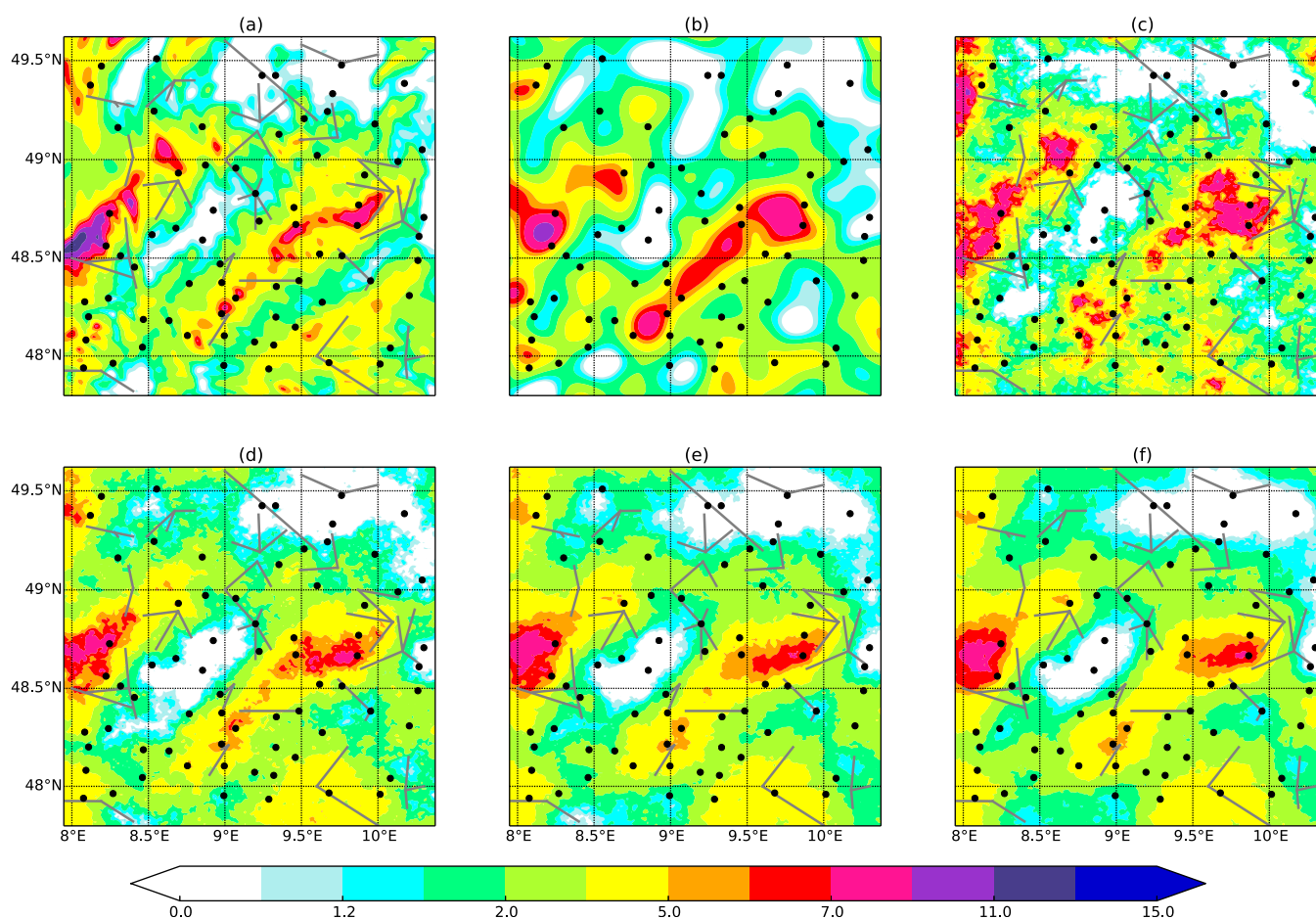


Figure 3. Comparison between the (a) VR precipitation field and (b–f) fields generated using Random Mixing exemplarily for the time step 31 May 2013 5 P.M. in mm/h: (a) VR precipitation field, (b) one single reconstruction based on rain gauge observations only, and (c) one single reconstruction based on the combined data set of rain gauge and CML observations. An interpolation of the combined data set from rain gauge and CML observations is shown, calculated as mean field based (d) on 5 random fields, (e) on 20 random fields, and (f) on 75 random fields. The black dots mark the locations of virtual rain gauges and the grey lines locations of virtual CMLs.

the virtual observations, we have simulated 75 random fields for each time step separately following the Random Mixing method. Each single random field is one possible reconstruction of the spatial rainfall field.

Figure 3 demonstrates the generation of precipitation fields using RM exemplarily for 5 P.M. on 31 May 2013. Figure 3a shows the VR reference field. The rainfall field shown in Figure 3b is an example for a single reconstruction which is in concordance with the rain gauge observations only. This means the field solves equation (5) to equation (7), but the CML observations are not used. A single random field which is in concordance with both, the rain gauge and CML measurements is shown in Figure 3c. This single reconstruction solves additionally also equation (9), hence the distance to the observed path-averaged rain rates \bar{R}_ξ is minimized. Comparing both fields (b, c) to the reference precipitation field of the VR (a), it can be seen both reconstructions mirror the main pattern, i.e., heavier precipitation in mountainous regions and the Alpine foothills (in the south of the domain) as well as drier regions in the North-East and the Neckar valley, fairly well. However, it can also be seen that the reconstruction, based on rain gauges only (Figure 3b), misses the smaller structures. This is likely a result of the limited spatial representativeness of rain gauges. Including CML observations into the reconstruction clearly improves the small-scale precipitation patterns (Figure 3c).

For this synthetic examples, we have simulated 75 single realizations (RM fields) as exemplarily depicted in Figure 3c. Since the CML observations are integral measures, describing a path-averaged rain rate, they do not give an unique solution for the reconstruction at the observed path. Furthermore, any RM precipitation field is only one selected possible solution of an infinite number. Depending on performance requirements, the outcome by using the Random Mixing can vary from single reconstructions, over ensembles of possible reconstructions, to observation-based interpolations on the basis of an ensemble of reconstructed precipitation fields. The second row of the figure shows the ensemble mean of 5 single realizations (d), 20 single realizations (e), and all 75 single realizations (f). A comparison with the VR precipitation shows that each ensemble mean reflects the main pattern of the VR reasonably well. However, while a single random field tends to be too noisy compared to the VR rainfall field, using an increasing number of random fields for the interpolation results in a more structured pattern, but then the extremes are smoothed. Therefore, the interpolation is highly dependent on the chosen quantity of random fields. In the following, we will reference the mean calculated over an ensemble of five single reconstructions (Figure 3d) as RM interpolation.

The dispersion of the 75 single realizations around the ensemble mean precipitation is expressed by the coefficient of variation. It is calculated as the ratio of the standard deviation to the mean. Figure 4 shows the coefficient of variation between the 75 possible precipitation reconstructions of the virtual example

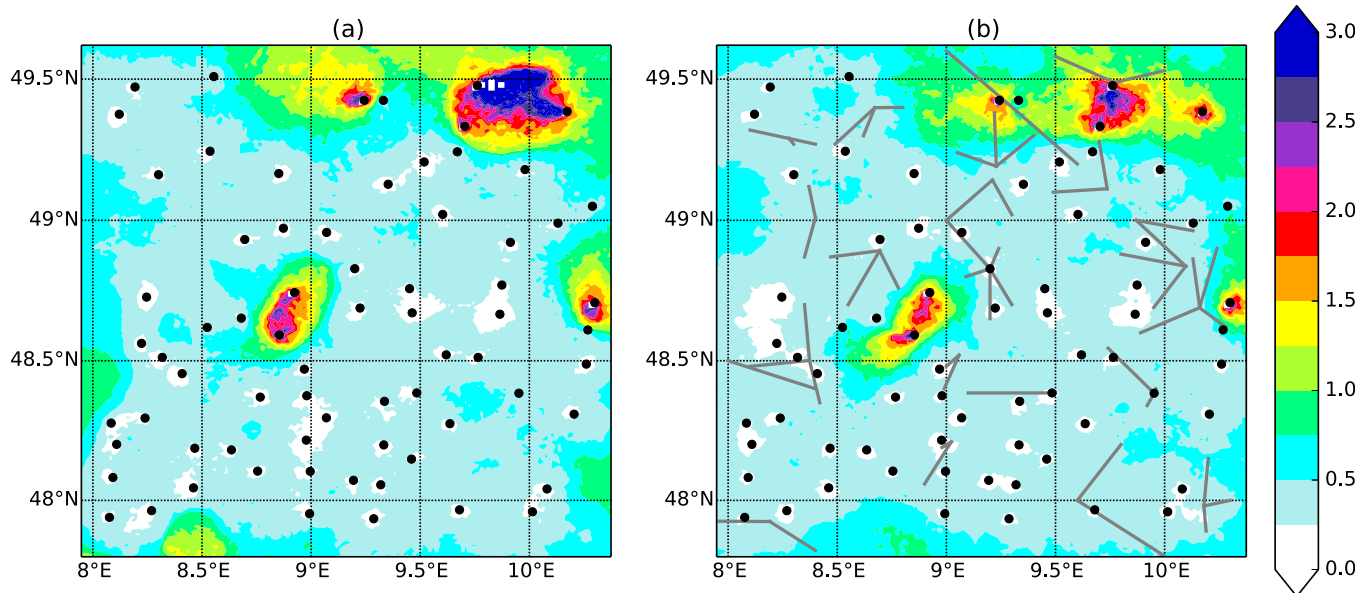


Figure 4. Coefficient of variation of all 75 single random fields generated using the Random Mixing method exemplarily for the time step 31 May 2013 5 P.M. in mm/h: (a) reconstructions based on rain gauge observations only and (b) reconstructions based on the combined data set of rain gauge and CML observations. The black dots mark the locations of virtual rain gauges and the grey lines locations of virtual CMLs.

based on rain gauges only (a) and based on the combined data consisting of rain gauges and CML observations (b). High values of the coefficient of variation indicate a high range of uncertainties relative to the precipitation amount and vice versa. For this time step, the coefficient of variation is relatively low over most of the catchment area. Only in the north-east of the catchment and south-west of Stuttgart (extending approximately from 48.5°N and 8.5°E to 48.8°N and 9°E) a higher coefficient of variation can be found. Using the combined observation data decreases the coefficient of variation over most of the area.

A direct comparison of the interpolation using OK against the interpolation using RM in respect to the VR (Figure 3a) is shown in Figure 5. Here the left column shows the interpolations using OK (a) and RM (c), the right column shows the difference plots of $OK - VR$ (b) and $RM - VR$ (d). Both methods reflect the main precipitation (left column) well with a slight underestimation of the mean value by 0.28 mm/h for OK and by 0.15 mm/h for RM. Moreover, the difference patterns in respect to the VR are comparable for both methods. The difference to the VR is for RM and OK less than ± 1 mm/h over most of the area. Only in the areas of higher precipitation, the Black Forest region (in the west of the domain) and the Swabian Alps, the interpolation using OK and the interpolation using RM show obvious differences. While OK underestimates

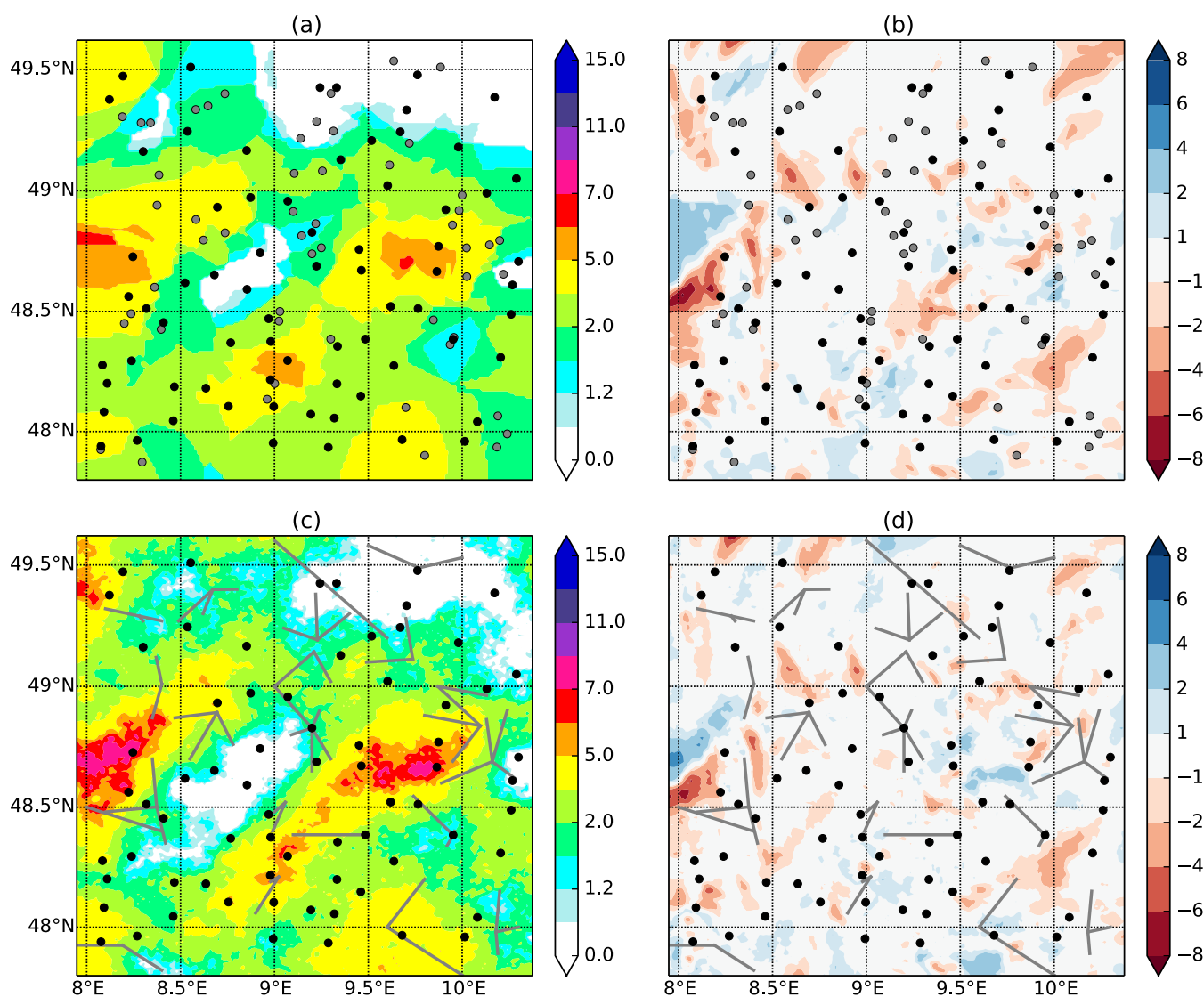


Figure 5. Comparison of interpolation using OK and RM exemplarily for the time step 31 May 2013 5 P.M. in mm/h. The interpolated precipitation field using OK resp. RM is depicted at left column (a) resp. (c). The right column shows the difference plots regarding to the VR, $OK - VR$ (b) resp. $RM - VR$ (d). The black dots mark the locations of virtual rain gauges. The locations of the virtual CML are marked in grey, (a and b) as dots for the paths center and (c and d) lines for the link path.

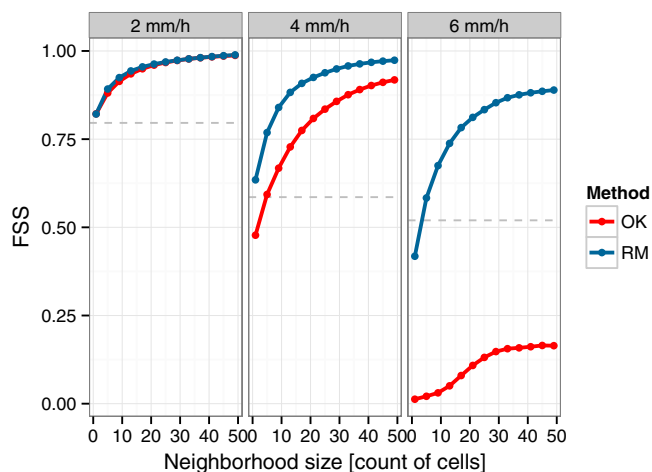


Figure 6. FSS for the interpolation using OK (red) and RM (blue) calculated for different sizes of neighborhoods for the thresholds of 2 mm/h (left), 4 mm/h (middle), and 6 mm/h (right) exemplarily for the time step 31 May 2013 5 P.M. The dashed line marks the cut-off point after which a reasonable skill has been achieved.

higher precipitation values by approx. 8.2 mm/h, the underestimation by RM is 7.5 mm/h. However, the Figures 5b and 5d do not show such remarkable differences among each other.

Since slight shifts of the pattern result in two errors (see Figure 5), an under as well as an overestimation located closely together (double penalty effect), we have calculated the FSS for different thresholds (Figure 6). While both methods show a mostly identical performance for a threshold of 2 mm/h, RM shows superior performance when using higher thresholds. For a threshold of 4 mm/h, RM has reached a reasonable skill at the used resolution of 1.1 km while OK reaches a reasonable skill at a resolution of 5.5 km corresponding to five grid cells. Using a threshold of 6 mm/h, RM reaches a reasonable performance at a resolution of approx. 4 km (four grid cells), while OK does not show a reasonable performance at all. This dominance of RM regarding the reconstruction of the higher thresholds is an advantage given by the method; using a linear combination of fields following the observed spatial dependence structure, instead of a pure interpolation method, allows the generation of extreme values between the observed ones.

The chronological sequence of the area mean precipitation of the VR (black), the interpolations using OK (red) and RM (solid blue line), one possible single reconstruction using RM (dashed blue line), and the spread between the 75 single realizations (RFs, blue shade) for the precipitation event are shown in Figure 7. It is demonstrated that its timing is well captured by both interpolations, using OK (red) or RM (blue), as well as by all single realizations. However, all precipitation fields generated using OK and nearly all fields generated using RM tend to a slight underestimation of the mean field precipitation over most of the period. Furthermore, the onset of the area mean precipitation of the reconstructions or interpolations has a delay of around 7 h when using RM, which results most likely from the construction itself. Since during the first 7 h only sparse rain showers occur, the virtual rain gauges do not catch these showers and consequently they are not included within the spatial distribution. OK instead, uses all measurements equally, hence the onset of the interpolation is nearly correct.

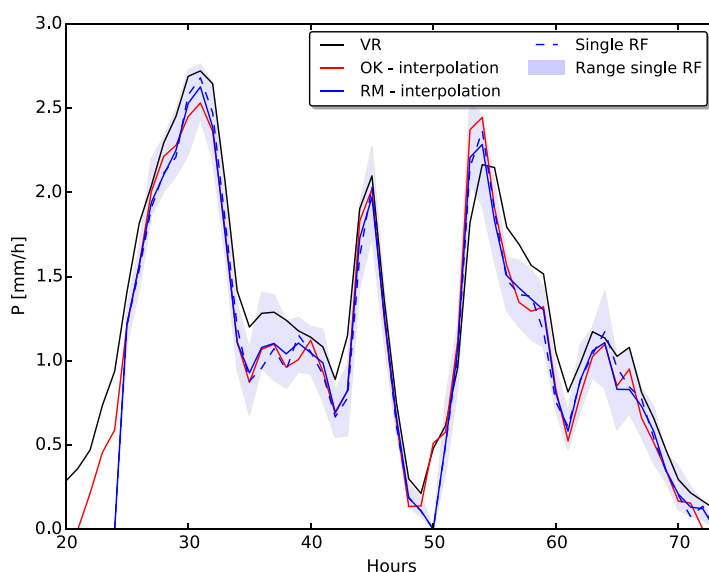


Figure 7. Area mean of hourly precipitation fields over the period of the precipitation event. The chronological sequence of the VR precipitation (black), the interpolation using OK (red), the interpolation using RM (solid blue line), one possible single reconstruction using RM (dashed blue line), and the spread between the 75 single realizations (RF, blue shade).

Figure 8 shows the interpolated rainfall using OK (b) and RM (c) accumulated over the period of the precipitation event compared to the accumulated VR precipitation (a). The accumulations of both interpolations as well as the VR reveal the typical summer precipitation pattern for the Neckar area, with the driest areas at north-west and wetter regions in mountainous regions as well as the Alpine foothills. Both interpolations show a dry bias in the areas of the Black Forest and the Swabian Alps compared to the VR. While this dry bias is constant over the whole area when using the RM, the interpolation using OK shows additionally a wet bias at the north-west part of the catchment area. The accumulated rainfall of the RM interpolation ranges between dry areas with 7 mm in the north-west and wet areas with 152 mm in the mountainous regions, it underestimates the VR precipitation which ranges from 13 to 205 mm. In contrast the OK interpolation has a smaller range between dry (14 mm) and wet areas (140 mm) as the VR. The area mean precipitation is with an amount of approx. 58 mm the same for both interpolation methods; both interpolation methods underestimate the area mean precipitation of the VR by approx. 10 mm.

The quality of the interpolated precipitation time series is also confirmed by Figure 9 on a hourly timescale for OK (a) and RM (b). It is shown that both interpolations fit the mean precipitation values fairly well, but tend to underestimate the extreme rainfall. While OK clearly

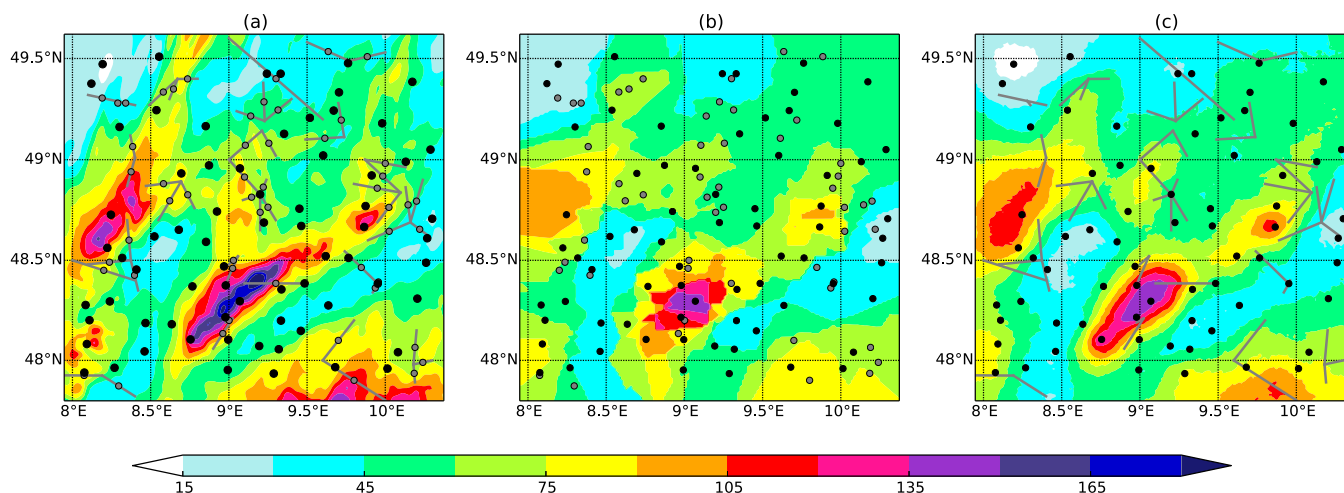


Figure 8. Accumulated precipitation pattern over the precipitation event in mm of (a) the VR, (b) the interpolation using OK, and (c) the interpolation using RM. The black dots mark the locations of virtual rain gauges. The locations of the virtual CML are marked in grey, (a and b) as dots for the paths center and (a and c) lines for the link path.

does not reproduce higher rainfall amounts, the underestimation of rainfall amounts is less intense when using RM. However the pixels of higher values for the RM interpolation are often slightly displaced (see also Figure 6). This is also verified by the correlation coefficient ρ , it is 0.8 when using RM and 0.7 when using OK. The coefficient of determination is 0.64 for RM and 0.48 for OK.

Summarizing, the virtual example demonstrates that the RM method is capable to generated ensembles of single reconstructions or interpolations, using rain gauge and CML precipitation observations, which reflect the spatial and temporal behavior of the known reference reasonably well. It has been shown that the dry bias in the extreme values has been reduced when using the interpolation with RM instead of OK. Also the spatial variation is, although pixel with extreme values are slightly displaced, well presented by the RM interpolation. This has been verified by the FSS. However, the precipitation fields generated using RM (reconstruction of single realizations or interpolation) exhibit a dry bias compared to the VR precipitation fields. One reason for the dry bias might be that the marginal distribution is estimated based on the rain

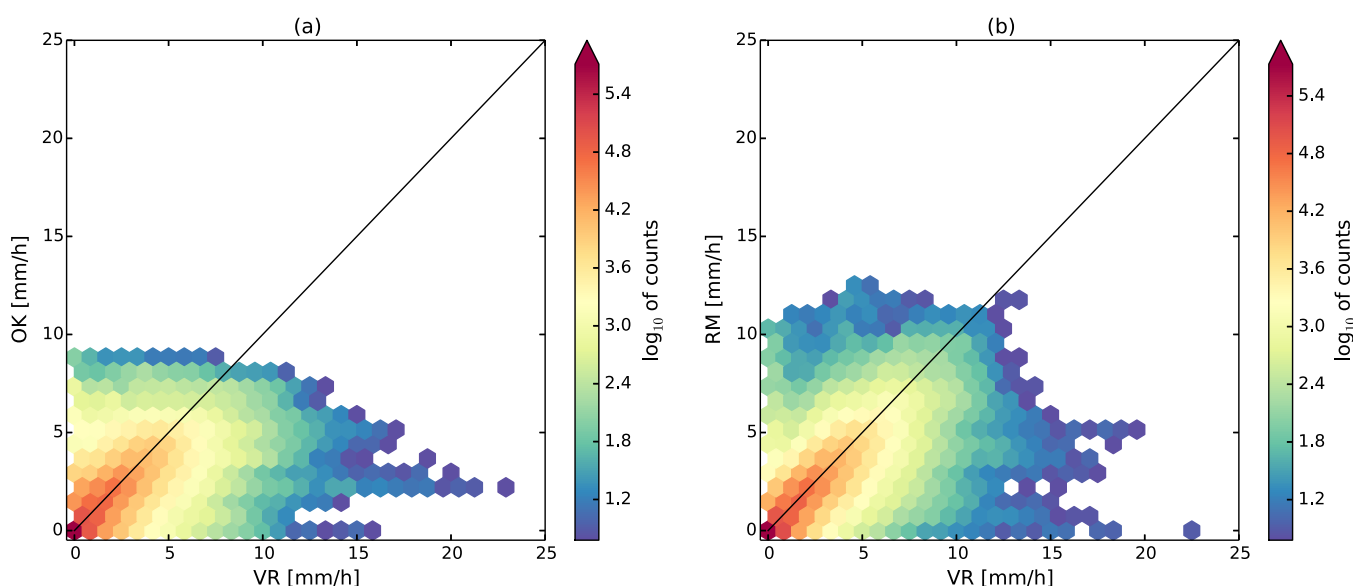


Figure 9. Pixel-wise (size: $\sim 1.1 \text{ km}^2$) validation of the interpolated precipitation against VR precipitation on an hourly basis for (a) OK and (b) RM over the whole simulation period. The black line denotes the 1:1 line.

gauges. Hence, if the rain gauge stations do not fully represent the frequency distribution, the method shows decreased performance (see also underestimation at Figure 8c or shifted onset at Figure 7).

4.2. Real-World Test Case

For demonstration of RM on real precipitation observations, we have chosen a 5 h precipitation event occurring over the study area located in Bavaria (see Figure 2 white solid box, red marks). This rain shower is moved from north-west of the study area southward. The observed time period of this precipitation event counts from 8 P.M. at 22 June 2015 until 12 A.M. at 23 June 2015. For this 5 h time period, we use the RM method to interpolate the combined set of precipitation observations, consisting of rain gauge and CML measurements (see section 3.2). Like in the previous section (section 4.1), the interpolation is calculated as

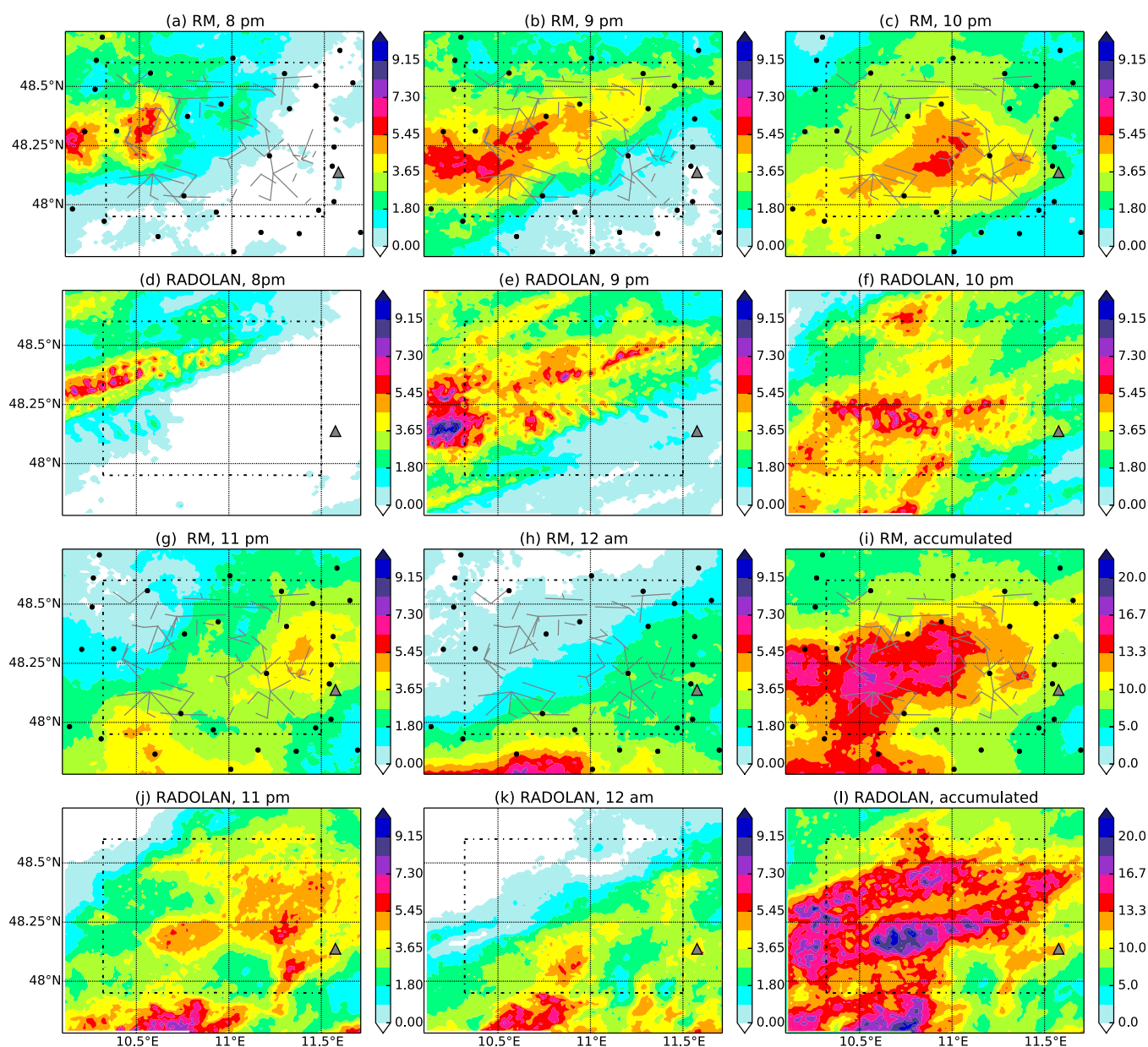


Figure 10. (a–c and g–i) Interpolated precipitation fields using RM, for the period 22 June 2015 8 P.M. to 23 June 2015 12 A.M., compared to (d–f and j–l) RADOLAN precipitation fields. Hourly precipitation fields are shown at (a–c and g, h) resp. (d–f and j, k) for the RM interpolation resp. the RADOLAN data set. The accumulated RM resp. RADOLAN precipitation is pictured at (i) resp. (l). The points and lines at the figures (a–c and g–i) mark the observations, rain gauges, and CMLs, which are used by RM. The dashed box marks the area where CML measurements are available and the grey triangle marks the location of the city of Munich.

the mean over five single reconstructions of the precipitation field. Subsequently, the interpolated time series of precipitation fields is evaluated against the corresponding RADOLAN data set (section 3.3).

Figure 10 shows the interpolated hourly precipitation fields using the RM method (a–c and g, h) compared to the precipitation fields of the RADOLAN data set (d–f and j, k). As in the virtual example, when comparing the RM interpolations with the corresponding RADOLAN fields, the interpolations capture the main precipitation pattern very well, but tend to underestimate the heavier precipitation values. The maximal hourly precipitation of the RADOLAN data ranges from 7.7 mm/h at 12 A.M. to 11 mm/h at 10 P.M. This is much higher than the range of the maximal hourly precipitation of the RM interpolation which is between 5 mm/h at 11 P.M. and 8.2 mm/h at 12 A.M. However, the area mean of the hourly precipitation over the interpolated area differs less than 1 mm/h compared to the corresponding area mean of the RADOLAN data. The interpolated mean values are slightly underestimating (overestimating) the RADOLAN data from 9 P.M. to 11 P.M. (8 P.M. and 12 A.M.). Furthermore, the precipitation fields of the RADOLAN data exhibit local minima-maxima patterns, this is particularly noticeable from 8 P.M. until 10 P.M. (Figures 10d–10f). These local minima-maxima patterns are most likely due to the limited temporal resolution, which induces this pattern for fast moving showers of rain. Since Random Mixing is not predisposed for this kind of uncertainties, the interpolations do not illustrate such local minima-maxima patterns.

Evaluating the pattern of the accumulated precipitation over the 5 h interval, both the RM interpolation (Figure 10i) and the RADOLAN (Figure 10l) main pattern are relatively similar. However, the underestimation of the interpolated high precipitation values is especially apparent for the accumulated pattern. While the accumulated precipitation of the interpolations ranges between 3.5 and 18 mm, the accumulation of the RADOLAN data ranges from 3.5 to 23 mm.

One reason for the underestimation can be found at the definition of Random Mixing: The marginal distribution and hence the spatial structure has been defined by the rain gauge observations. In case that the CML observations indicate high precipitation amounts and if simultaneously this high precipitation amounts are not reflected by the rain gauge observations, the resulting single reconstructions can have high uncertainties around the CML observations. An example for such a case is the precipitation field at 9 P.M. While the interpolation smoothed out the extreme values of the area from 48 to 48.5°N and 10 to 10.5°E (Figure 10b versus Figure 10e), the five single reconstructions do indicate high precipitation values (example single reconstruction Figure 11a), but the exact locations differ between the single

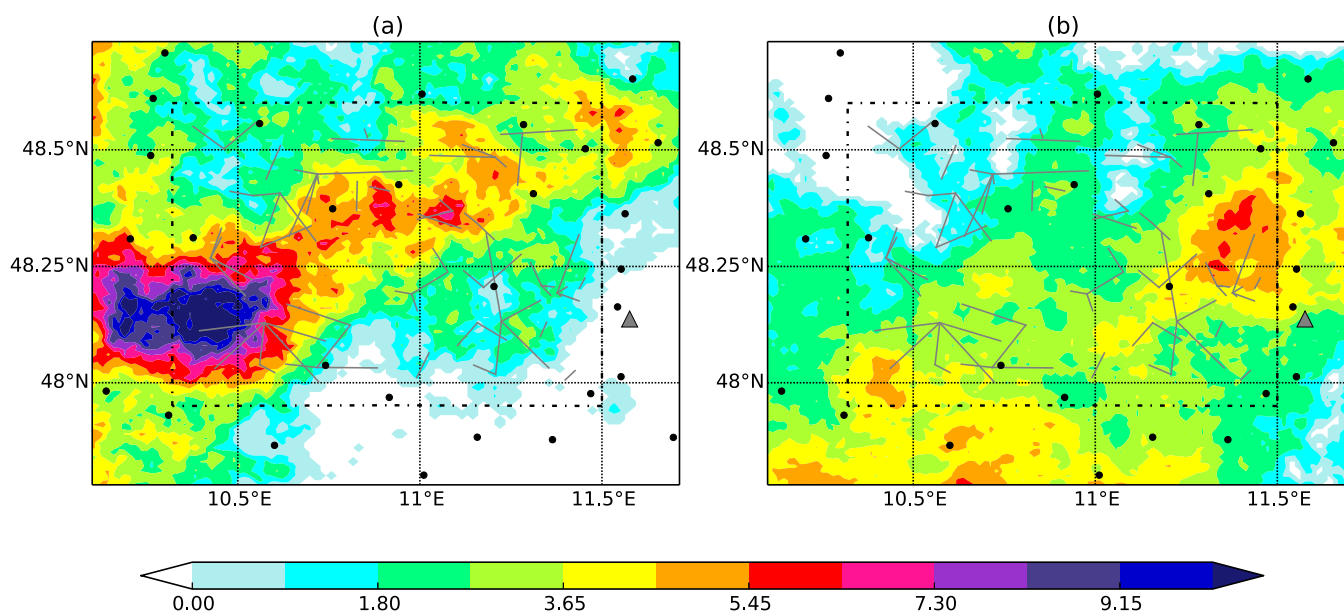


Figure 11. Single random fields of reconstructed precipitation for 22 June 2015 (a) 9 P.M. and (b) 11 P.M.. The points and lines at the figures mark the observations, rain gauges, and CMLs, which are used by Random Mixing. The dashed box marks the area where CML measurements are available and the grey triangle marks the location of the city of Munich.

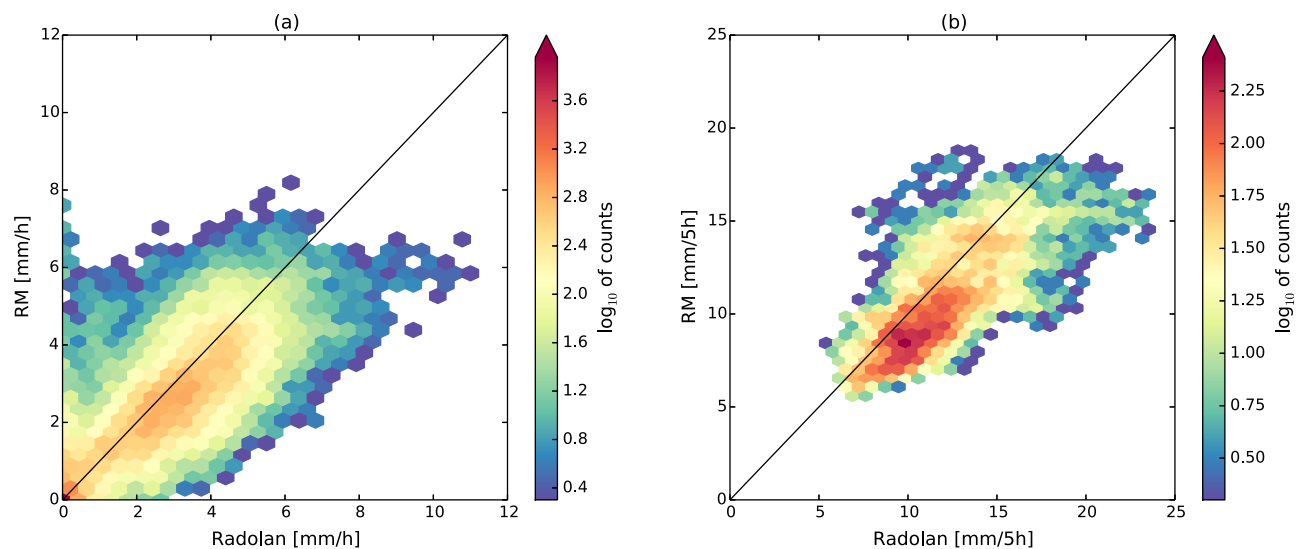


Figure 12. Pixel-wise (size: $\sim 1.1 \text{ km}^2$) validation of the (a) RM interpolation against the RADOLAN data on an hourly basis and (b) for the accumulated precipitation of the 5 h precipitation event. The black line denotes the 1:1 line.

reconstructions. Another possibility is shown e. g., in Figure 10g versus Figure 10j. Here, the rain gauges are also not reflecting high precipitation values and the path-averaged rain rate given by the CML observations include no particularly high precipitation amounts. Hence, the corresponding single reconstructions do not include the higher precipitation amounts (Figure 11b).

The pixel-wise comparison of the interpolation with the RADOLAN data is shown in Figure 12. The hourly comparison (Figure 12a) shows an overall agreement between pixels of the interpolation and RADOLAN data set, which is also shown by a correlation coefficient of 0.84 and coefficient of determination of 0.70. As seen earlier for the spatial pattern, RM tends to underestimate the count of precipitation pixels, especially the pixels of high values. There is only a small number of pixels in which the RM interpolation overestimates the RADOLAN data. Furthermore, a mismatch of dry RADOLAN pixels, in which the RM interpolation indicates precipitation, is detected. However, the mean precipitation per pixel is very similar between the RM interpolation (2.09 mm/h) and the RADOLAN data (2.34 mm/h). Considering the pixel-wise comparison of the accumulated precipitation (Figure 12b), the underestimation of the RADOLAN pattern by the RM pattern can also be seen. Here, the RADOLAN mean value (11.7 mm) is underestimated by more than 1 mm by RM (10.5 mm). Likewise the accumulated interpolation has a well pixel-wise performance, with a correlation coefficient (coefficient of determination) of 0.75 (0.56). However, both the correlation coefficient and coefficient of determination are lower as the ones in the hourly evaluation. One reason might be the lower variation of accumulated precipitation amounts of the interpolation compared to the RADOLAN data (Figure 10i and 10l).

Summarizing, this example demonstrates that Random Mixing generates precipitation fields in a good quality compared to the RADOLAN data set. One has to be aware that both the interpolation using RM and also the corresponding RADOLAN data set are based on the same rain gauge data, which might result in an unrealistic high correlation. Nevertheless, since the RADOLAN data are a widely used gridded data set for hourly precipitation, we decided to use it as the reference for the real-world example.

5. Conclusions and Perspectives

This study presents the first application of the RM method to reconstruct or interpolate precipitation fields on the basis of a combined data set, consisting of rain gauge and CML observations. RM constrains directly on the CML information, without any transformation into pixel data. The resulting reconstructed precipitation fields are in concordance with the rain gauge and CML observations and additionally reflect the observed rainfall variability along the CML paths. We have demonstrated the approach on both a virtual as well as a real-world data set. Both examples show that RM is capable to simulate single reconstructions,

Table 1

Summary of Quality Measures to Test the Performance of Random Mixing (RM) and Ordinary Kriging (OK) for a Single Time Step (Exemplarily for 31 May 5 pm) as Well as the Whole Precipitation Event

Method	RMSE (mm/h)	ρ	r^2
RM (31 May 5 P.M.)	1.07	0.77	0.59
OK (31 May 5 P.M.)	1.20	0.71	0.50
RM	1.14	0.8	0.64
OK	1.65	0.7	0.48

respectively, interpolations of the target precipitation pattern in a good quality. A pixel by pixel comparison between the interpolated time series of the virtual observational data set and the virtual reality results in a Pearson correlation coefficient of 0.8. The pixel-wise comparison of the time series of the real-world example yields even a Pearson correlation coefficient of 0.84.

Utilizing the synthetic example, the RM interpolation has a comparable high quality as the established method introduced by Overeem et al. (2013). The quality measures RMSE, correlation coefficient (ρ), and the coefficient of determination (r^2) of RM and OK evaluated against the VR are very similar, with a slight improvement if using RM

(Table 1). An apparent improvement of the similarity of the neighborhood evaluated against the VR has been demonstrated by using RM in comparison to OK. The improvement is in particular present for higher precipitation values. It has been shown that the marginal distribution estimated on the basis of the rain gauges is a reasonable estimate, which otherwise most likely causes the underestimation of precipitation amounts. This is particularly noticeable for extreme precipitation amounts or onsets of rainy periods. Thus one future enhancement of the methodology could be the consideration of CML observations for the estimation of both, the marginal distribution $F(r)$ and spatial copula model. This could be realized by incorporating a nonparametric merging approach as proposed by e. g., Hasan et al. (2016b) for the combination of rain gauge and radar observations, into the RM algorithm.

Due to the construction details, one distinctive feature of RM is its capability to generate ensembles of any desired size. We have shown that each ensemble member solves the constraints given by the observations. This ensemble generation enables the estimation of the uncertainty of the observation-based reconstruction. In particular, since RM uses the observed path-averaged CML-derived rain rate directly, the variability in rainfall intensity along the link path can be estimated. Moreover, a well-known approach for hydrological forecasts is data assimilation, which requires a large ensemble of rainfall fields as input. RM mixing represents a novel approach to create such arbitrarily large ensembles relatively fast and requiring relatively low computational power.

In this study, the spatial dependence of the precipitation fields is described using Gaussian copulas. However, in reality the spatial dependence structure of precipitation might not be symmetric. This asymmetry can be seen especially at locations with extreme precipitation values. For an improved representation of the strong dependence in extreme values, the application of a nonmonotonic transformation of the Gaussian copula (e.g., AghaKouchak et al., 2010; Bárdossy & Li, 2008; Haslauer et al., 2012; Hörning, 2016) can be an alternative. Since precipitation amount is related to the topography, further improvement could be obtained by the incorporation of topographic information into the spatial dependence structure of precipitation (Bárdossy & Pegram, 2013).

Appendix A: Setup Details

When running the RM algorithm one has to choose the number of the first set of addends of the linear combinations utilized at equations (5) and (7). The n which has been used at equation (5) for the quasi-interpolation has to be greater than the number of rain gauge observations (K) in order to get an underconstrained system of equations. Hence, we define the starting value of n with $n_0 := K + \lfloor 0.5 \cdot K \rfloor$. If n has to be increased, the next n_{i+1} is $n_{i+1} := n_i + \lfloor 0.5 \cdot K \rfloor$. The counter J , with $J > K$, has been defined similar, with a start value $J_0 := K + 20$ and $J_{i+1} := J_i + 20$.

The threshold ε of equation (9) is defined for each time step separately. It is depending on the CML derived path-averaged rain rates \bar{R}_ξ (the number of CMLs is Ξ) and is set as $\varepsilon = 0.5 \cdot (\min_{\xi \in \{1, \dots, \Xi\}} (\bar{R}_\xi))$.

The full synthetic data set used in section 4.1 can be obtained from Haese and Schalge (2017). It consists of synthetic rain gauge observations and CML-derived path-averaged rain rates, as well as the reference precipitation fields. At the current state, it is not possible to publish the metadata of the locations of the real-world CML paths. Since this metadata are necessary for the usage of the CML observations, we do not publish the CML-derived path-averaged rain rates.

Acknowledgments

The authors acknowledge the DWD Climate Data Center (CDC) for providing the rain gauge data and the RADOLAN RW product for this study. Rain gauge and radar data used in this work can be obtained after registration from the CDC (<ftp-cdc.dwd.de>). This work is funded by Deutsche Forschungsgemeinschaft (DFG) as part of the project "Geostatistical Analysis and Copula-Based Data Merging Algorithms for a Stochastic Quantification of Precipitation Fields" within the research unit FOR2131 (Data Assimilation for Improved Characterization of Fluxes across Compartmental Interfaces) and as part of the project "Integrating Microwave Link Data For Analysis of Precipitation in Complex Terrain: Theoretical Aspects and Hydrometeorological Applications" (IMAP).

References

- AghaKouchak, A., Bárdossy, A., & Habib, E. (2010). Conditional simulation of remotely sensed rainfall data using a non-Gaussian v-trans-formed copula. *Advances in Water Resources*, 33(6), 624–634. <https://doi.org/10.1016/j.advwatres.2010.02.010>
- Andrieu, H., Creutin, J. D., Delrieu, G., & Faure, D. (1997). Use of a weather radar for the hydrology of a mountainous area. Part I: Radar measurement interpretation. *Journal of Hydrology*, 193(1), 1–25. [https://doi.org/10.1016/S0022-1694\(96\)03202-7](https://doi.org/10.1016/S0022-1694(96)03202-7)
- Baldauf, M., Seifert, A., Förstner, J., Majewski, D., Raschendorfer, M., & Reinhardt, T. (2011). Operational convective-scale numerical weather prediction with the COSMO model: Description and sensitivities. *Monthly Weather Review*, 139(12), 3887–3905. <https://doi.org/10.1175/MWR-D-10-05013.1>
- Bárdossy, A., & Hörning, S. (2015). Random mixing: An approach to inverse modeling for groundwater flow and transport problems. *Transport in Porous Media*, 1–19. <https://doi.org/10.1007/s11242-015-0608-4>
- Bárdossy, A., & Li, J. (2008). Geostatistical interpolation using copulas. *Water Resources Research*, 44, W07412. <https://doi.org/10.1029/2007WR006115>
- Bárdossy, A., & Pegram, G. (2013). Interpolation of precipitation under topographic influence at different time scales. *Water Resources Research*, 49, 4545–4565. <https://doi.org/10.1002/wrcr.20307>
- Bartels, H., Weigl, E., Reich, T., Lang, P., Wagner, A., Kohler, O., & Gerlach, N. (2004). *Abschlussbericht Projekt RADOLAN* (technical report). Offenbach, Germany: Deutscher Wetterdienst.
- Berne, A., & Uijlenhoet, R. (2007). Path-averaged rainfall estimation using microwave links: Uncertainty due to spatial rainfall variability. *Geophysical Research Letters*, 34, L07403. <https://doi.org/10.1029/2007GL029409>
- Bianchi, B., van Leeuwen, J. P., Hogan, R. J., & Berne, A. (2013). A variational approach to retrieve rain rate by combining information from rain gauges, radars, and microwave links. *Journal of Hydrometeorology*, 14(6), 1897–1909. <https://doi.org/10.1175/JHM-D-12-094.1>
- Chwala, C., Gmeiner, A., Qiu, W., Hipp, S., Nienaber, D., Siart, U., . . . Kunstmann, H. (2012). Precipitation observation using microwave back-haul links in the alpine and pre-alpine region of Southern Germany. *Hydrology and Earth System Sciences*, 16, 2647–2661. <https://doi.org/10.5194/hess-16-2647-2012>
- Chwala, C., Keis, F., & Kunstmann, H. (2016). Real-time data acquisition of commercial microwave link networks for hydrometeorological applications. *Atmospheric Measurement Techniques*, 9(3), 991–999. <https://doi.org/10.5194/amt-9-991-2016>
- D'Amico, M., Manzoni, A., & Solazzi, G. L. (2016). Use of operational microwave link measurements for the tomographic reconstruction of 2-D maps of accumulated rainfall. *IEEE Geoscience and Remote Sensing Letters*, 13(12), 1827–1831. <https://doi.org/10.1109/LGRS.2016.2614326>
- Doumounia, A., Gosset, M., Cazenave, F., Kacou, M., & Zougmore, F. (2014). Rainfall monitoring based on microwave links from cellular telecommunication networks: First results from a West African test bed. *Geophysical Research Letters*, 41, 6015–6021. <https://doi.org/10.1002/2014GL060724>
- DWD Climate Data Center (CDC) (2016). *Historische stündliche Stationsmessung der Niederschlagshöhe, version v004*. Offenbach, Germany: DWD Climate Data Center (CDC).
- Frei, C., Christensen, J. H., Déqué, M., Jacob, D., Jones, R. G., & Vidale, P. L. (2003). Daily precipitation statistics in regional climate models: Evaluation and intercomparison for the European Alps. *Journal of Geophysical Research*, 108(D3), 4124. <https://doi.org/10.1029/2002JD002287>
- Germann, U., Galli, G., Boscacci, M., & Bolliger, M. (2006). Radar precipitation measurement in a mountainous region. *Quarterly Journal of the Royal Meteorological Society*, 132(618), 1669–1692. <https://doi.org/10.1256/qj.05.190>
- Giuli, D., Facheris, L., & Tanelli, S. (1999). Microwave tomographic inversion technique based on stochastic approach for rainfall fields monitoring. *IEEE Transactions on Geoscience and Remote Sensing*, 37(5), 2536–2555. <https://doi.org/10.1109/36.789649>
- Giuli, D., Toccafondi, A., Gentili, G. B., & Freni, A. (1991). Tomographic reconstruction of rainfall fields through microwave attenuation measurements. *Journal of Applied Meteorology*, 30(9), 1323–1340. [https://doi.org/10.1175/1520-0450\(1991\)030<1323:TRORFT>2.0.CO;2](https://doi.org/10.1175/1520-0450(1991)030<1323:TRORFT>2.0.CO;2)
- Goldstein, O., Messer, H., & Zinevich, A. (2009). Rain rate estimation using measurements from commercial telecommunications links. *IEEE Transactions on Signal Processing*, 57(4), 1616–1625. <https://doi.org/10.1109/TSP.2009.2012554>
- Goudenhoofd, E., & Delobbe, L. (2009). Evaluation of radar-gauge merging methods for quantitative precipitation estimates. *Hydrology and Earth System Sciences*, 13(2), 195–203. <https://doi.org/10.5194/hess-13-195-2009>
- Haese, B., & Schälge, B. (2017). Supplement_Stochastic_Reconstruction_and_Interpolation_of_Precipitation_Fields_Using_Combined_Information_CML_and_RG [Data set]. Zenodo. Retrieved from <https://doi.org/10.5281/zenodo.846639>
- Hasan, M. M., Sharma, A., Johnson, F., Mariethoz, G., & Seed, A. (2016a). Merging radar and in situ rainfall measurements: An assessment of different combination algorithms. *Water Resources Research*, 52, 8384–8398. <https://doi.org/10.1002/2015WR018441>
- Hasan, M. M., Sharma, A., Mariethoz, G., Johnson, F., & Seed, A. (2016b). Improving radar rainfall estimation by merging point rainfall measurements within a model combination framework. *Advances in Water Resources*, 97, 205–218. <https://doi.org/10.1016/j.advwatres.2016.09.011>
- Haslauer, C. P., Guthke, P., Bárdossy, A., & Sudicky, E. A. (2012). Effects of non-Gaussian copula-based hydraulic conductivity fields on macrodispersion. *Water Resources Research*, 48, W07507. <https://doi.org/10.1029/2011WR011425>
- Hazenbergh, P., Leijnse, H., & Uijlenhoet, R. (2011). Radar rainfall estimation of stratiform winter precipitation in the Belgian Ardennes. *Water Resources Research*, 47, W02507. <https://doi.org/10.1029/2010WR009068>
- Hörning, S. (2016). *Process-oriented modeling of spatial random fields using copulas* (dissertation, Report Nr. 246). Stuttgart, Germany: Institut für Wasser- und Umweltsystemmodellierung, Universität Stuttgart. <https://doi.org/10.18419/opus-8871>
- Hu, L. Y. (2000). Gradual deformation and iterative calibration of Gaussian-related stochastic models. *Mathematical Geology*, 32(1), 87–108. <https://doi.org/10.1023/A:1007506918588>
- Jameson, A. R. (1991). A comparison of microwave techniques for measuring rainfall. *Journal of Applied Meteorology*, 30(1), 32–54. [https://doi.org/10.1175/1520-0450\(1991\)030<0032:ACOMTF>2.0.CO;2](https://doi.org/10.1175/1520-0450(1991)030<0032:ACOMTF>2.0.CO;2)
- Joss, J., & Pittini, A. (1991). Real-time estimation of the vertical profile of radar reflectivity to improve the measurement of precipitation in an Alpine region. *Meteorology and Atmospheric Physics*, 47(1), 61–72. <https://doi.org/10.1007/BF01025828>
- Kühnlein, M., Appelhans, T., Thies, B., & Nauss, T. (2014). Improving the accuracy of rainfall rates from optical satellite sensors with machine learning: A random forests-based approach applied to MSG SEVIRI. *Remote Sensing of Environment*, 141, 129–143. <https://doi.org/10.1016/j.rse.2013.10.026>
- Laux, P., Vogl, S., Qiu, W., Knoche, H. R., & Kunstmann, H. (2011). Copula-based statistical refinement of precipitation in RCM simulations over complex terrain. *Hydrology and Earth System Sciences*, 15(7), 2401–2419. <https://doi.org/10.5194/hess-15-2401-2011>
- Lawrence, P. J., & Chase, T. N. (2007). Representing a new MODIS consistent land surface in the Community Land Model (CLM 3.0). *Journal of Geophysical Research*, 112, G01023. <https://doi.org/10.1029/2006JG000168>

- Leijnse, H., Uijlenhoet, R., & Stricker, J. (2008). Microwave link rainfall estimation: Effects of link length and frequency, temporal sampling, power resolution, and wet antenna attenuation. *Advances in Water Resources*, 31, 1481–1493. <https://doi.org/10.1016/j.advwatres.2008.03.004>
- Liberman, Y., & Messer, H. (2014a). *Accurate reconstruction of rain field maps from Commercial Microwave Networks using sparse field modeling*. Paper presented at 2014 IEEE International Conference on Acoustics, Speech and Signal Processing (ICASSP), (pp. 6786–6789), IEEE, Florence, Italy. <https://doi.org/10.1109/ICASSP.2014.6854914>.
- Liberman, Y., Samuels, R., Alpert, P., & Messer, H. (2014b). New algorithm for integration between wireless microwave sensor network and radar for improved rainfall measurement and mapping. *Atmospheric Measurement Techniques*, 7(10), 3549–3563. <https://doi.org/10.5194/amt-7-3549-2014>
- Mao, G., Vogl, S., Laux, P., Wagner, S., & Kunstmann, H. (2015). Stochastic bias correction of dynamically downscaled precipitation fields for Germany through Copula-based integration of gridded observation data. *Hydrology and Earth System Sciences*, 19, 1787–1806. <https://doi.org/10.5194/hess-19-1787-2015>
- Messer, H., Zinevich, A., & Alpert, P. (2006). Environmental monitoring by wireless communication networks. *Science*, 312(5774), 713–713. <https://doi.org/10.1126/science.1120034>
- Nelsen, R. (1999). *An introduction in copulas*. New York, NY: Springer.
- Nešpor, V., & Sevruk, B. (1999). Estimation of wind-induced error of rainfall gauge measurements using a numerical simulation. *Journal of Atmospheric and Oceanic Technology*, 16(4), 450–464. [https://doi.org/10.1175/1520-0426\(1999\)016<0450:EOWIEO>2.0.CO;2](https://doi.org/10.1175/1520-0426(1999)016<0450:EOWIEO>2.0.CO;2)
- Olsen, R., Rogers, D., & Hodge, D. (1978). The aR b relation in the calculation of rain attenuation. *IEEE Transactions on Antennas and Propagation*, 26(2), 318–329.
- Overeem, A., Leijnse, H., & Uijlenhoet, R. (2011). Measuring urban rainfall using microwave links from commercial cellular communication networks. *Water Resources Research*, 47, W12505. <https://doi.org/10.1029/2010WR010350>
- Overeem, A., Leijnse, H., & Uijlenhoet, R. (2013). Country-wide rainfall maps from cellular communication networks. *Proceedings of the National Academy of Sciences United States of America*, 110(8), 2741–2745. <https://doi.org/10.1073/pnas.1217961110>
- Overeem, A., Leijnse, H., & Uijlenhoet, R. (2016). Retrieval algorithm for rainfall mapping from microwave links in a cellular communication network. *Atmospheric Measurement Techniques*, 9(5), 2425–2444. <https://doi.org/10.5194/amt-9-2425-2016>
- Philipp, A., Kerl, F., Büttner, U., Metzkes, C., Singer, T., Wagner, M., & Schütze, N. (2016). Small-scale (flash) flood early warning in the light of operational requirements: Opportunities and limits with regard to user demands, driving data, and hydrologic modeling techniques. *Proceedings of the International Association of Hydrological Sciences*, 373, 201–208. <https://doi.org/10.5194/piahs-373-201-2016>
- Randall, D. A., Wood, R. A., Bony, S., Colman, R., Fichet, T., Fyfe, J., . . . Taylor, K. E. (2007). Climate models and their evaluation. In *Climate change 2007: The physical science basis. Contribution of working group I to the fourth assessment report of the IPCC (FAR)* (pp. 589–662), Cambridge, UK: Cambridge University Press.
- Roberts, N. M., & Humphrey, W. L. (2008). Scale-selective verification of rainfall accumulations from high-resolution forecasts of convective events. *Monthly Weather Review*, 136(1), 78–97. <https://doi.org/10.1175/2007MWR123.1>
- Roy, V., Gishkori, S., & Leus, G. (2014). *Spatial rainfall mapping from path-averaged rainfall measurements exploiting sparsity*. Paper presented at 2014 IEEE Global Conference on Signal and Information Processing (GlobalSIP) (pp. 321–325). Atlanta, GA: IEEE. <https://doi.org/10.1109/GlobalSIP.2014.7032131>
- Schleiss, M., & Berne, A. (2010). Identification of dry and rainy periods using telecommunication microwave links. *IEEE Geoscience and Remote Sensing Letters*, 7(3), 611–615. <https://doi.org/10.1109/LGRS.2010.2043052>
- Seo, D. J., & Breidenbach, J. P. (2002). Real-time correction of spatially nonuniform bias in radar rainfall data using rain gauge measurements. *Journal of Hydrometeorology*, 3(2), 93–111. [https://doi.org/10.1175/1525-7541\(2002\)003<0093:RTCOSN>2.0.CO;2](https://doi.org/10.1175/1525-7541(2002)003<0093:RTCOSN>2.0.CO;2)
- Serinaldi, F. (2009). Copula-based mixed models for bivariate rainfall data: An empirical study in regression perspective. *Stochastic Environmental Research and Risk Assessment*, 23(5), 677–693. <https://doi.org/10.1007/s00477-008-0281-z>
- Sevruk, B., & Zhlavova, L. (1994). Classification system of precipitation gauge site exposure: Evaluation and application. *International Journal of Climatology*, 14(6), 681–689. <https://doi.org/10.1002/joc.3370140607>
- Smiatek, G., Keis, F., Chwala, C., Fersch, B., & Kunstmann, H. (2017). Potential of commercial microwave link network derived rainfall for river runoff simulations. *Environmental Research Letters*, 12(3), 034026. <https://doi.org/10.1088/1748-9326/aa5f46>
- Smiatek, G., Kunstmann, H., & Senatore, A. (2016). EURO-CORDEX regional climate model analysis for the Greater Alpine Region: Performance and expected future change. *Journal of Geophysical Research: Atmosphere*, 121, 7710–7728. <https://doi.org/10.1002/2015JD024727>
- Thorndahl, S., Nielsen, J. E., & Rasmussen, M. R. (2014). Bias adjustment and advection interpolation of long-term high resolution radar rainfall series. *Journal of Hydrology*, 508, 214–226. <https://doi.org/10.1016/j.jhydrol.2013.10.056>
- Ulbrich, C. W., & Lee, L. G. (1999). Rainfall measurement error by WSR-88D radars due to variations in ZR law parameters and the radar constant. *Journal of Atmospheric and Oceanic Technology*, 16(8), 1017–1024. [https://doi.org/10.1175/1520-0426\(1999\)016<1017:RMEBWR>2.0.CO;2](https://doi.org/10.1175/1520-0426(1999)016<1017:RMEBWR>2.0.CO;2)
- Vogl, S., Laux, P., Qiu, W., Mao, G., & Kunstmann, H. (2012). Copula-based assimilation of radar and gauge information to derive bias-corrected precipitation fields. *Hydrology and Earth System Sciences*, 16(7), 2311–2328. <https://doi.org/10.5194/hess-16-2311-2012>
- Wagner, A., Seltmann, J., & Kunstmann, H. (2012). Joint statistical correction of clutters, spokes and beam height for a radar derived precipitation climatology in southern Germany. *Hydrology and Earth System Sciences*, 16(11), 4101–4117. <https://doi.org/10.5194/hess-16-4101-2012>
- Weijenborg, C., Friederichs, P., & Hense, A. (2015). Organisation of potential vorticity on the mesoscale during deep moist convection. *Tellus Series A*, 67(1), 25705. <https://doi.org/10.3402/tellusa.v67.25705>
- Zinevich, A., Alpert, P., & Messer, H. (2008a). Estimation of rainfall fields using commercial microwave communication networks of variable density. *Advances in Water Resources*, 31(11), 1470–1480. <https://doi.org/10.1016/j.advwatres.2008.03.003>
- Zinevich, A., Messer, H., & Alpert, P. (2008b). Frontal rainfall observation by a commercial microwave communication network. *Journal of Applied Meteorology and Climatology*, 48(7), 1317–1334. <https://doi.org/10.1175/2008JAMC2014.1>
- Zinevich, A., Messer, H., & Alpert, P. (2010). Prediction of rainfall intensity measurement errors using commercial microwave communication links. *Atmospheric Measurement Techniques*, 3(5), 1385–1402. <https://doi.org/10.5194/amt-3-1385-2010>